Review of Scientific Instruments

X-ray imaging detector for radiological applications adapted to the context and requirements of low- and middle-income countries

Mario Andrés Chavarria, Matthias Huser, Sebastien Blanc, et al.

View Online　　**Export Citation**　　**CrossMark**

ARTICLES YOU MAY BE INTERESTED IN

Review of Scientific Instruments

Read Now!

Special Issue: Advances in Measurements and Instrumentation Leveraging Embedded Systems

X-ray imaging detector for radiological applications adapted to the context and requirements of low- and middle-income countries

Mario Andrés Chavarria,[1,a] Matthias Huser,[2] Sebastien Blanc,[1] Pascal Monnin,[3] Jérôme Schmid,[4] Christophe Chênes,[4] Lazhari Assassi,[4] Hubert Blanchard,[5] Romain Sahli,[5] Jean Philippe Thiran,[6] René Salathé,[7] and Klaus Schönenberger[1,a]

AFFILIATIONS

[1] EssentialTech Centre, Ecole Polytechnique Fédérale de Lausanne (EPFL), Lausanne CH-1015, Switzerland
[2] Ecole Technique–Ecole des Métiers–Lausanne (ETML), Lausanne CH-1004, Switzerland
[3] Institute of Radiation Physics (IRA), Lausanne University Hospital (CHUV) and University of Lausanne (UNIL), Lausanne CH-1007, Switzerland
[4] Geneva School of Health Sciences, HES-SO University of Applied Sciences and Arts Western Switzerland, Genève CH-1206, Switzerland
[5] Pristem S.A., Lausanne CH-1007, Switzerland
[6] Signal Processing Laboratory 5, Ecole Polytechnique Fédérale de Lausanne (EPFL), Lausanne CH-1015, Switzerland
[7] School of Engineering, Ecole Polytechnique Fédérale de Lausanne (EPFL), Lausanne CH-1015, Switzerland

[a] Authors to whom correspondence should be addressed: mario.chavarria@epfl.ch and klaus.schonenberger@epfl.ch

ABSTRACT

This paper describes the development of a novel medical x-ray imaging system adapted to the needs and constraints of low- and middle-income countries. The developed system is based on an indirect conversion chain: a scintillator plate produces visible light when excited by the x rays, and then, a calibrated multi-camera architecture converts the visible light from the scintillator into a set of digital images. The partial images are then unwarped, enhanced, and stitched through parallel field programmable gate array processing units and specialized software. All the detector components were carefully selected focusing on optimizing the system's image quality, robustness, cost-effectiveness, and capability to work in harsh tropical environments. With this aim, different customized and commercial components were characterized. The resulting detector can generate high quality medical diagnostic images with detective quantum efficiency levels up to 60% (@2.34 μGy), even under harsh environments, i.e., 60 °C and 98% humidity.

I. INTRODUCTION

According to the World Health Organization (WHO), more than two thirds of the world's population does not have access to essential x-ray imaging equipment.[1] This "global radiology gap" does not attract as much attention as infectious-disease outbreaks or natural disasters, but it can be as dangerous to the public health and can affect "the entire global health care system."[2] Too often in low- and medium-income countries (LMICs), patients die of trivial problems, which could not be treated properly, or were left untreated, due to a lack of access to proper diagnosis. Road accidents, tuberculosis, and complications from childhood pneumonia are recurrent examples of pathologies causing complications that could have been prevented with functional and efficient x-ray imaging services.[3] Even when there are x-ray systems available, a majority are obsolete, based on technologies from 50 years ago or older, such as film-based

systems.[2,4] This generates high operating costs and often yields a poor image quality.[5]

Commonly, when addressing the issue of access to medical technology in LMICs, the main considered factor is the economy, i.e., the purchasing cost. This leads to "well intended" donations of medical equipment that is not adapted to the local context. Such donations are not only useless but they can also "actively inhibit healthcare delivery and further burden healthcare providers."[6] As a result, "medical equipment graveyards" of obsolete or broken donated biomedical equipment are commonly seen in hospitals across LMICs.[6,7]

To address this problem, the GlobalDiagnostiX project aims at developing, in partnership with local actors in Cameroon, digital, ultra-robust, and affordable radiological x-ray equipment adapted to the needs and constraints of LMICs. Our methodology[8] relies on three pillars: (1) cooperation and co-creation with local stakeholders in Cameroon (user centered design), (2) interdisciplinarity, with the participation of engineers, radiologists, radiographers, anthropologists, designers, etc., and (3) entrepreneurship, as the output of the academic work provided the basis for an award-winning start-up company.

A. Field study: Cameroon

Cutting-edge technology is often designed for high-income countries and is expected to work in LMICs. This common and erroneous assumption has led to products that do not work properly nor do they have the intended impact, and if they do work at first, the implementation and maintenance effort and costs are usually so high that they rapidly fall into disuse.[9,10] To avoid this issue, the first phase of the project included a field study in Cameroon to define the requirements and expectations of all stakeholders in the pilot country. With this aim, we analyzed the available x-ray medical imaging systems available in the country's healthcare system (Fig. 1) and interviewed stakeholders form all the stages of the x-ray technology chain, i.e., physicians, radiographers, medical equipment distributors, biomedical engineers, academic institutions, NGOs, inspectors, and different officials from the ministry of public health of Cameroon (MPHC). The results of this study and videos of some of the interviews are presented in

FIG. 1. X-ray imaging equipment observed in the field study in Cameroon: The equipment in this hospital dates from the 1970s and poses a serious safety risk as the dose of radiation can no longer be measured (©Sylvain Liechti, EPFL2015).

the documentary "X-Ray Machines: Africa's Broken System"[7] and the "Technology Innovation for Sustainable Development" [Massive Open Online Course (MOOC)].[11] Based on the feedback from the stakeholders and the studied literature, the main points to address during the development of the x-ray imaging system are as follows:

- Digitalization: Over the last decade, digitalization has played a prominent role in the x-ray medical equipment. Film-based and Computed Radiography (CR) plates are being replaced by fully digital x-ray detectors, requiring a lower amount of dose and providing a better image quality in a very short amount of time. In addition, digital technology enables video capabilities, which has given rise to new applications, such as fluoroscopy, cone beam computed tomography (CBCT), and tomosynthesis. However, due to the mismatch between existing solutions and the local context, modern digital x-ray systems are not widely available in LMICs.
- Cost-effectiveness: This should apply to the total cost of ownership, e.g., operation costs and maintenance costs, not just the purchasing price.
- Robustness: Endemic problems of the local context, such as the lack of quality infrastructure, i.e., lack of stable electrical power, which tends to cause frequent and extended downtimes, and the scarcity of trained personnel to use and maintain the devices, are an important cause of a reduced lifespan of the x-ray equipment.[5] Additionally, the harsh environment, which involves high levels of humidity and high temperatures, causes high failure rates. The performance and lifespan of digital x-ray equipment, detectors especially, are prone to be compromised at a high humidity rate and temperatures.[5] During our field study, we received multiple reports from health personnel in Sub-Saharan countries that the quality of the x-ray images is degraded when temperature increases above a certain level. Some radiographers even reported that due to this effect, they stopped performing radiographies when temperatures were above "27 or so" degrees Celsius.
- Maintenance and reparability: The lack of replacement parts and the scarcity of trained personnel to do maintenance and repair the devices when they need it highly reduce the utility and lifespan of the few available devices.

B. State-of-the-art

The most common architectures for x-ray digital detectors are flat panels and multi-camera array detectors. Flat panels provide a high image quality, i.e., detective quantum efficiency (DQE) values from 40% to 75%, depending on the configuration and components, which lead to a reduction in the required exposure times and radiation dose rates.[12–16] However, a major drawback of the flat panel technology is the cost (production, maintenance, and replacement).[12] Flat panel detectors utilize advanced semiconductor components that require costly cleanroom manufacturing processes, which leads to high eventual costs for the final product. Although there are some examples of low cost flat panel solutions in the literature, they usually have a lower image quality, i.e., DQE values from 20% to ~35%, or do not provide enough information for a

precise comparison.[12,17–19] Furthermore, in addition to the purchasing costs, flat panels have high maintenance/repairing costs, e.g., if damaged, the whole detector should be replaced by a specialist at a considerable cost. The complexity of the technology also mandates maintenance and repair by specialized personnel, who are not commonly available in LMICs.

The alternatives to flat panels are the multi-camera array detectors, such as the IONA from TeleOptic or the Naomi from RFSystems. These systems generate the images using a scintillator and an array of cameras. Unlike flat panels, the multi-camera detectors do not use large, brittle semiconductor substrates but small image sensors. Therefore, they are more robust and can be produced at a lower cost.[20,21] However, their lower optical coupling leads to an increase in image noise and a decrease in detective efficiency, i.e., DQE levels from 20% to 40%.[22–26]

Commercially available detectors, both flat panels and multi-camera array detectors, usually require ambient temperatures of ~25 °C and maximum operating temperatures of 35 °C at relative humidity levels between 30% and 70%.[15,16,27] This is a limiting factor for their implementation in many regions in Africa, and other LMICs, where the average temperatures regularly exceed 35 °C, even sometimes reaching temperatures of more than 50 °C, and the relative humidity reaches levels of ≥80%.[28–33]

C. Proposed solution

The limitations of flat panel technology (e.g., price, fragility, and lack of reparability) set the multi-camera array based detector a better option for the targeted market. This type of architecture allowed more freedom to design a detector adapted to the needs and constrains of LMICs, such as lower fabrication and maintenance costs, easier maintenance, and improved reparability by using "off the shelf" components, which can be easily obtained and replaced on the field, high robustness under harsh environmental conditions, among others.

The developed system implements innovative real-time hardware electronics that comprises multiple Complementary Metal Oxide Semiconductor (CMOS) image sensors. Each image sensor provides a partial image, and all the captured partial images need to be pre-processed and combined using specialized software running on an array of parallel processing field programmable gate array (FPGA) units. The image acquisition and processing electronics were designed in easily replaceable modules to reduce the

complexity of maintenance and repair and to improve the cost efficiency of the solution, i.e., avoiding the need to replace the complete detector if one of its components breaks.

The proposed x-ray detector is based on indirect conversion [Fig. 2]: the x-ray photons hit a scintillator screen that emits multiple visible photons upon absorption. These secondary photons form a visible image that is then captured by an array of cameras. Finally, dedicated electronic and computing units such as FPGA chips collect the data from the sensors and send a reconstructed image to an external computer for visualization.

The main components of the indirect x-ray conversion chain are:

Scintillator: The scintillator is a key element in the conversion chain. It converts x rays to visible photons with high efficiency and very low lateral scattering. When an x-ray photon hits an atom of the scintillating material, an electron from the inner orbital is ejected. Surrounding electrons with higher energy will take the empty place by releasing excess of energy with multiple photons at lower energy (in the range of 2–2.5 eV, visible spectra).[34,35]

Indirect conversion digital x-ray detectors for medical applications often implies one of two types of scintillator materials: cesium iodide (CsI:Tl) or gadolinium oxysulfide (Gd$_2$O$_2$S:Tb). Both have advantages and disadvantages regarding light throughput, resolution, price, resistance to temperature and humidity, etc.

Lenses: The lens has the role of collecting the visible photons and making them converge to an image sensor, with as little optical aberrations and distortion as possible. Its importance in the conversion chain is not to be neglected: a low quality lens (i.e., aberration and low transmission rate) leads to bad optical coupling, low modulation transfer function (MTF), and DQE. The specifications of the lens (i.e., focal length and aperture) define the magnification factor (or field of view), which has a direct impact on the minimum distance between the scintillator and the sensor to have a good overlap between the sub-images.

Image sensors: Image sensors are semiconductor chips that embed an array of photodiodes and some integrated electronics to drive and control this array. The designed detector implements off-the-shelf CMOS image sensors to reduce fabrication costs and to ensure easy access to replacement parts. CMOS sensors have several advantages compared to the Thin-Film-Transistor (TFT) technology, commonly used in x-ray flat panel detectors.[13,17,36] CMOS sensors can be mass-produced, using standard manufacturing techniques, significantly reducing their costs. CMOS sensors
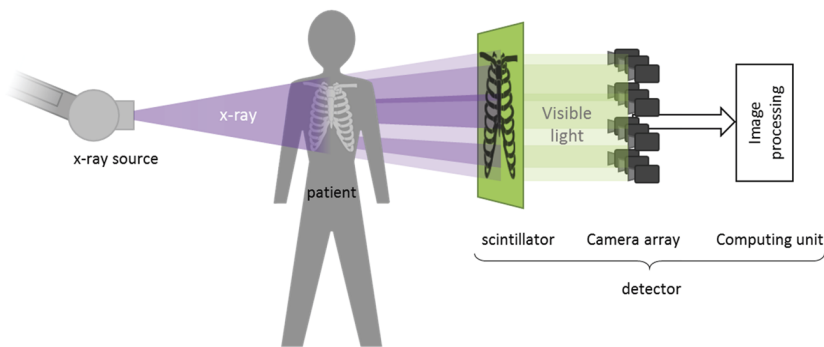

FIG. 2. Schematic of the detector's indirect x-ray conversion chain.

have low power consumption and offer very fast image acquisition. The CMOS technology benefits of silicon substrates offering the best performances and state-of-the-art semiconductor technologies. Additionally, the implemented CMOS sensors are less sensitive to temperature and can operate at higher temperatures than other image sensor technologies.[36] On the other hand, the active area of the CMOS sensor is typically much smaller than the active area from flat panel sensors. Therefore, lenses are used for projection and demagnification of the scintillator image. This reduces the optical coupling, leading to a reduction in the final DQE.

During the development phase, each section of the conversion chain was tested using different commercial elements in order to define an optimal set of components to achieve state-of-the-art clinical images under harsh environment conditions. This also provides information about possible replacement parts in case one of the components stop being produced or is not available in the implementation country. Each of the selected components, the development and characterization process and the implemented system architecture, is described in detail in Secs. II–VI.

II. MATERIALS AND METHODS

A. Characterized components

1. Scintillators

In order to identify the best x-ray conversion device, in terms of performance and cost, several scintillators (CsI:Tl and Gd_2O_2S:Tb) from different manufacturers were analyzed. After a preselection, based on the active area, thickness, and resolution, seven models of commercial scintillators were acquired for characterization. Table I lists the selected scintillators with their main features.

2. Lenses

Although commercial lenses have a multitude of different mount designs in the machine vision industry, there are three widely used formats, i.e., C-mount, CS-mount, and S-mount (also called M12). After a careful analysis of the different lens mountings, the S-mount lenses were selected for the detector design due to their small size, flexibility, low maintenance, and cost efficiency. Once the mount type was selected, nine of the most suitable lenses were purchased for characterization (Table II).

Since the lenses present different specifications (e.g., focal length) and design, the field of view is different for each lens. Therefore, the working distance for each lens was set to have a similar

TABLE I. Characterized commercial scintillators with their main features.

Scintillator	Origin	Technology	Size (mm)	Thickness (μm)
SC1(CI)	Japan	Csi:Tl	430 × 430	400
SC2(CI)	China	Csi:Tl	430 × 430	400
SC3(GOS)	Japan	Gd_2O_2S:Tb	430 × 430	140
SC4(GOS)	Japan	Gd_2O_2S:Tb	430 × 430	208
SC5(GOS)	China	Gd_2O_2S:Tb	430 × 430	390
SC6(GOS)	UK	Gd_2O_2S:Tb	430 × 430	250
SC7(GOS)	UK	Gd_2O_2S:Tb	430 × 430	250

TABLE II. Characterized lenses with their main features.

Lens	Origin	Focal length (mm)	F-stop	Sensor type	Working distance (mm)
L1	Germany	6	1.6	1/2.5	102
L2	Germany	6	1.6	1/2	100
L3	China	6	1.2	1/2.7	97
L4	China	2.8	1.2	1/2.7	55
L5	China	3.6	1.2	1/2.7	68
L6	Germany	6	1.6	1/2	100
L7	Germany	16	1.6	1/2	267
L8	Germany	6	1.2	1/3	105
L9	Germany	8	1.2	1/3	138

image size on the scintillator to that of the reference configuration, i.e., L2 lens @100 mm. This allows comparing the lenses' efficiency with a fixed camera density for a 43×43 cm^2 image size, which is the usual size for a general-purpose medical detector. The determined working distances of all the lenses are summarized in the last column of Table II.

3. Image sensors

The market was screened for cost efficient CMOS image sensors with a suitable resolution. Color image sensors use Bayer filters to discriminate photons of a certain wavelength (color). Since the scintillator light is monochromatic (green), only 50% of the sensor pixels will be able to capture the generated image, i.e., the other 50% of the pixels (with red and blue filters) will not be able to capture any light. This significantly reduces the light transmission and, therefore, the overall sensitivity of the detector. Therefore, the monochrome image sensors represent the best fit for this application. On the other hand, color sensors are more demanded and, thus, usually more readily available and for a better price. Therefore, a set of two monochrome and two color sensors was selected, based on the manufacturer specifications, for an extensive comparison according to the EMVA 1288 3.1 standard.[37] The key selection parameters were signal-to-noise ratio (SNR) and sensitivity performance under low light conditions. The selected image sensors, and their main features, are presented in Table III.

The characterization of the IS3 monochrome and IS4 color sensors was performed using the evaluation boards provided by the manufacturer. For the IS1 (monochrome) and IS2 (color) sensors, commercial cameras were used.

TABLE III. Characterized sensors with their main features.

| Image sensor	Origin	Technology	Color	Resolution	Size
IS1	Japan	Back illuminated	Monochrome	1936 × 1096	1/2.8″
IS2	Japan	Back illuminated	Color	1936 × 1096	1/2.8″
IS3	USA	Front illuminated	Monochrome	1280 × 960	1/3″
IS4	USA	Front illuminated	Color	1928 × 1088	1/2.7″

4. Sensor shield

The scintillators do not absorb all the x-ray radiation from the source (the transmission rate varies depending on the type of scintillator and the x-ray spectra). The transmitted x-ray photons interact with all the components behind the scintillator, i.e., the mechanical support, the lenses, the image sensor, and the neighboring electronics.

X-ray tests show that the impact of the residual x-ray photons on the image sensor is non-negligible. Part of the residual x-ray photons are absorbed by the image sensor pixels, resulting in very high pixel values (PVs) in some localized areas (denominated "direct hits"), as exemplified in Fig. 3. From a medical point of view, the number of direct hits can highly affect the ability to perform a good medical diagnostic, i.e., the white spot artifacts can hide small features, thus valuable information.

A software solution can be applied to filter out the white spots by detecting and replacing the affected pixels with neighboring pixel values. However, correcting a very high number of direct hits may alter the image and lose too much information for a correct medical diagnosis. Therefore, to avoid losing information, a hardware solution must be added to protect the sensor, in addition to a software-based image correction (Sec. IV C 1).

Lead glass has high x-ray absorption efficiency, and it is transparent to visible light. Therefore, placing a lead glass shield between the scintillator and the camera can absorb the residual x rays while letting the visible light pass through. X-ray absorbance is linked to the concentration of Pb in the glass, usually given in "Pb equivalent thickness." However, these Pb atoms tend to tint the glass yellow, thus filtering some of the visible light. In order to reach a good trade-off between x-ray absorbance and light transmittance, two types of tests were performed with several Pb equivalent thickness glasses:

- **Hit count:** Measurements with shields with Pb equivalent thicknesses from 0 to 3.5 mm and source voltages from 50 to 200 kV were taken. An advanced threshold algorithm was developed to detect and count the number of direct hits in the obtained images (Sec. IV C 1).
- **X-ray absorption:** Light transmittance of shields, with Pb equivalent thicknesses from 0 to 3.5 mm, was measured for the wavelength range of 500–600 nm.
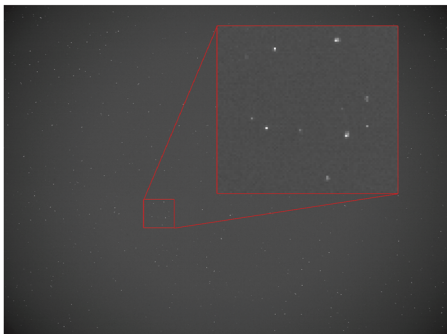
FIG. 3. Examples of direct hits (white spots) on a test image taken with no lead glass (@80 kV 30 mA s).

B. Image quality assessment

1. X-ray characterization

The assessment of image quality required the measurement of the MTF, the noise power spectrum (NPS), and the DQE.[38]

a. X-ray imaging setup and beam qualities. The detector was characterized for the standard beam quality RQA5 (70 kV—additional filtration of 21 mm Al at the tube exit) defined in the IEC 62220-1 document.[39] A scintillator was positioned 100 mm in front of the sensors, and a lead glass of equivalent thickness of 1.5 mm lead was interposed behind the scintillator to avoid direct detection by the pixels. The source-to-scintillator distance was set at 132 cm. Pre-processed digital images in a raw 16-bit format were used. The exposure time was varied to give different detector air kerma (DAK). All the images were obtained without an antiscatter grid. Air kerma measurements were made with a Radcal 9015 dosimeter (Radcal, Monrovia, CA) with a 6 cm^3 ionizing chamber. A standard air kerma value of 2.5 μGy was taken as the reference dose level at the detector. Several other target DAK between 0.59 and 18.7 μGy were analyzed.

b. System response. Uniform images acquired at different DAK were used to measure the relationship between the mean pixel value (PV) and the DAK. Regions of interest (ROIs) were selected at the center of each image for calculating the mean pixel value. The system response curve was fitted using a linear function,

$$PV = a + b \cdot DAK, \tag{1}$$

where a and b are fitted coefficients. The response curve was used to express the image pixel values into DAK levels for the MTF and NPS calculations.

c. Modulation transfer function (MTF). The MTF assesses the spatial resolution of the imaging system. The limit in resolution is often given as the spatial frequency at which the MTF value is equal to 5%.[40]

For this study, a tungsten sharp edge was imaged to produce the edge spread function (ESF). The derivative of the ESF gave the line spread function (LSF), the impulse response of the imaging system. The MTF is the magnitude of the Fourier transform of the LSF.[41]

Unless otherwise stated, all images for the MTF measurements were acquired using a RQA5 beam with a SC5(GOS) scintillator, L2 lenses, and the monochromatic sensor IS1, at a source-to-scintillator distance of 140 mm. A lead glass shield of 1.5 mm Pb equivalent was inserted between the scintillator and the camera to prevent the residual x rays from reaching the camera.

d. Noise power spectrum (NPS). The NPS describes the frequency content of the image noise. The 2D NPS is the magnitude squared of the Fourier transform of a homogeneous ROI on the image that contains only noise,

$$NPS(f_x, f_y) = \frac{1}{A} \left\langle \left| \iint_A \left(d(x,y) - \bar{d} \right) e^{-i2\pi(xf_x + yf_y)} dx dy \right|^2 \right\rangle, \tag{2}$$

where A is the area of the image, $d(x,y)$ is the pixel value at position (x, y), f_x and f_y are spatial frequencies in the x and y directions, respectively, and $\bar{d}$ is the mean pixel value in the ROI. The NPS was

calculated from three identical homogeneous images for each DAK. The normalized noise power spectrum (NNPS) $NNSP(f_x, f_y)$ is the NPS normalized by the square of the mean pixel value,

$$NNPS(f_x, f_y) = \frac{NPS(f_x, f_y)}{\overline{d}^2}. \quad (3)$$

1D NPS curves are radial averages of the 2D NPS, excluding the $0°$ and $90°$ axial values.

e. Detective quantum efficiency (DQE). The DQE quantifies the efficiency of the detector to convert incident x-ray photons into digital information. A high DQE value allows using less patient dose for the same image quality. Consequently, optimizing the DQE is a major concern in the design of x-ray detectors. The DQE is the ratio between the output signal-to-noise ratio squared (SNR_{out}^2) and the input signal-to-noise ratio squared (SNR_{in}^2) in the spatial frequency space,[39–42]

$$DQE = \frac{SNR_{out}^2}{SNR_{in}^2}. \quad (4)$$

The DQE is comprised between 0 and 1, 1 being a lossless detector. The DQE is proportional to the square of the MTF and inversely proportional to the NNPS and x-ray photon fluence (Q),

$$DQE(f_x, f_y) = \frac{MTF(f_x, f_y)^2}{NNPS(f_x, f_y) \cdot Q}. \quad (5)$$

The photon fluence (Q) is given by the product of the DAK and the x-ray fluence per unit DAK (φ),

$$Q = DAK \cdot \varphi \left[\frac{\#photons}{mm^2} \right]. \quad (6)$$

The spectral x-ray fluence per DAK is the number of x-ray photons per surface unit per dose unit [#photons/(mm² μGy)] and depends on the x-ray beam spectrum (kV and filtration).[39]

f. Spectroscopy. In order to precisely identify the requirements of the imaging sensor, spectroscopy measurements were performed in all the scintillators to determine their emitted light spectrum. Due to the low sensitivity of the spectrometer, high voltage (140 kV) and high dose (160 mA s) were applied, and no filter was added at the output of the tube during these tests.

2. Visible light characterization

To study the performance of image sensors in detail without interferences from external systems (e.g., scintillator and x-ray source), the image sensors and the developed detection system were tested under visible light. All image sensors were characterized without optics under darkroom conditions. A 525 nm green LED—a wavelength as close as possible to that of the scintillator—was selected as the light source. The light source was diffused with an integrating sphere to achieve the most homogeneous illumination of the sensor. The distance between the sphere output and the sensor plane was set to 100 mm. The irradiation of the source was measured with a calibrated photodiode and set to 1.0 μW/cm² (at the sensor plane). Each sensor was set at the smallest gain that achieved the highest pixel reading at saturation to ensure that the full dynamic range is used. A schematic of the implemented measurement setup is shown in Fig. 4.
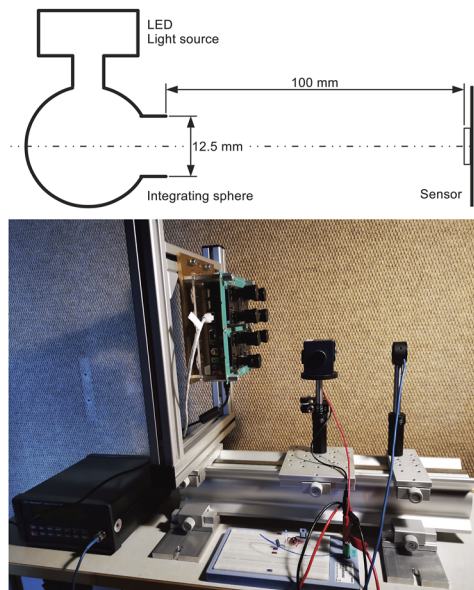

FIG. 4. Schematic and picture of the image sensors' characterization setup.

Based on the EMVA1288 standard, different series of images were shot with varying exposure time and constant illumination. Sets of two images were captured with exposure increasing linearly up to pixel saturation with 50 steps; a first series was shot with the light source ON and the second in total darkness. Subsequently, two additional series of 50 images were shot with illumination and exposure times corresponding to 50% of the pixel saturation value. Again, the first series was shot with the light source ON and the second in the dark. Finally, the data from the captured images were processed in order to extract the sensor's intrinsic parameters, e.g., quantum efficiency (QE), gain (K), signal-to-noise ratio (SNR_{MAX}), and dynamic range.

III. COMPONENTS' CHARACTERIZATION RESULTS

A. Scintillators

The selected scintillators were characterized using the methods described in Sec. II B—"Image quality assessment."

1. MTF

The measured MTF curves of all tested scintillators are shown in Fig. 5. As a result of its intrinsic micro-pillar structure, CsI:Tl scintillators are known to have very good spatial resolution in comparison to other types of scintillator (e.g., Gd_2O_2S:Tb). This is reflected in the excellent behavior observed with the SC1(CI) scintillator, leading to high MTF values at low and high spatial frequencies with the best measured cutoff frequency (4.52 lp/mm). The other CsI:Tl scintillator, SC2(CI), shows relatively low MTF values at low spatial frequencies but recovers after 2 lp/mm, reaching a cutoff frequency of 4.07 lp/mm.

The Gd_2O_2S:Tb scintillators were expected to show lower MTF levels than the CsI:Tl scintillators due to their powder structure.
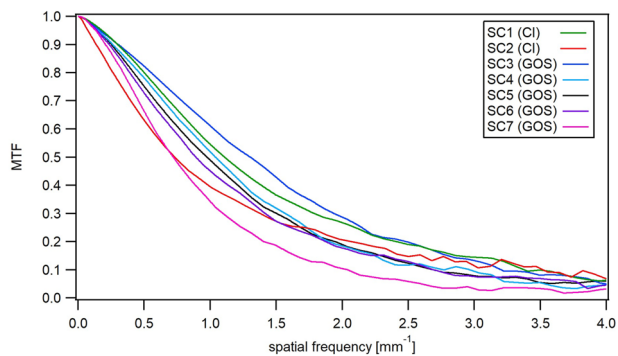
FIG. 5. MTF curves of all the tested scintillators under RQA5, 1.5 mm Pb equivalent lead glass.

Surprisingly, the SC3(GOS) obtained the highest MTF at low spatial frequencies. However, its MTF rapidly decreases above 2 lp/mm, which leads to a cutoff frequency of 3.99 lp/mm. The SC5(GOS) showed an average behavior at low and medium spatial frequencies. Nevertheless, its MTF remains almost flat at high frequency, leading to the second highest high cutoff frequency from the measured scintillators, i.e., 4.28 lp/mm. The SC7(GOS) has very poor MTF levels, probably due to its higher thickness compared to the other Gd_2O_2S:Tb scintillators. It only reached a 2.6 lp/mm cutoff frequency, below the minimum 2.8 lp/mm required for film-screen x-ray detectors intended to radiological applications.

2. DQE

The calculated DQE curves of all tested scintillators are compared in Figs. 6. Due to its high thickness and absorption rate, the SC1(CI) scintillator has the highest low-frequency DQE. The SC2(CI) shows relatively poor performance for a CsI:Tl scintillator. Surprisingly, the SC5(GOS), a low cost Gd_2O_2S:Tb scintillator, produced the third highest DQE levels among the measured scintillators. The SC7(GOS) outperforms the SC2(CI) and the SC5(GOS) with a DQE(0) of 18.4%. The high DQE(0) levels of the SC5(GOS)
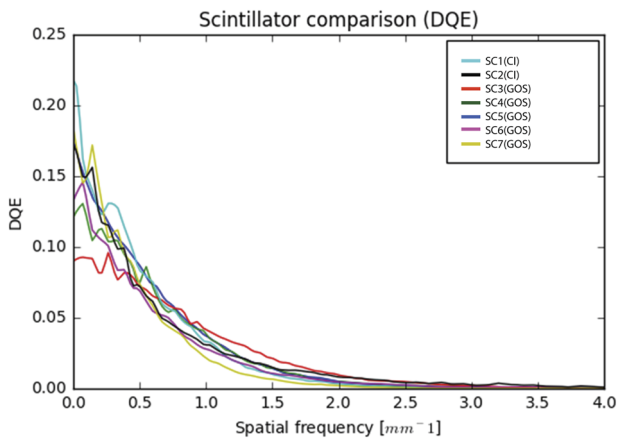
and the SC7(GOS) can be explained by their thicker active layer, i.e., higher absorption. However, higher thickness can lead to a poorer MTF, due to more lateral diffusion in the scintillating layer. This is especially critical in the case of SC6(GOS) and SC7(GOS).

3. NNPS vs temperature

The x-ray detector will operate in harsh environments, where ambient temperature can reach up to 45 °C with 100% relative humidity. The Gd_2O_2S:Tb scintillators are known to be very robust and stable; however, the CsI:Tl can suffer from image quality loss at high temperatures and humidity.[43] The impact of the temperature on image noise (NNPS) was measured for two scintillators at different temperatures, i.e., the SC3(GOS) (Gd_2O_2S:Tb) and SC2(CI) (CsI:Tl). The resulting NNPS curves are shown in Fig. 7.

As expected, the SC3(GOS) exhibits no change over the tested temperature range. Conversely, the SC2(CI) exhibits an increase in the NNPS by about 10% at high temperature (>45 °C). Since the NNPS is inversely proportional to the DQE, this would lead to a 10% decrease in DQE when used at a temperature over 45 °C.

4. Spectroscopy

The CsI:Tl scintillators have a very broad emission bandwidth (from ~470 to 640 nm); thus, the peak value is lower compared to Gd_2O_2S:Tb. All Gd_2O_2S:Tb scintillators exhibit a high peak emission at around 545 nm and few other peaks at around 490, 580, and 620 nm (Fig. 8).
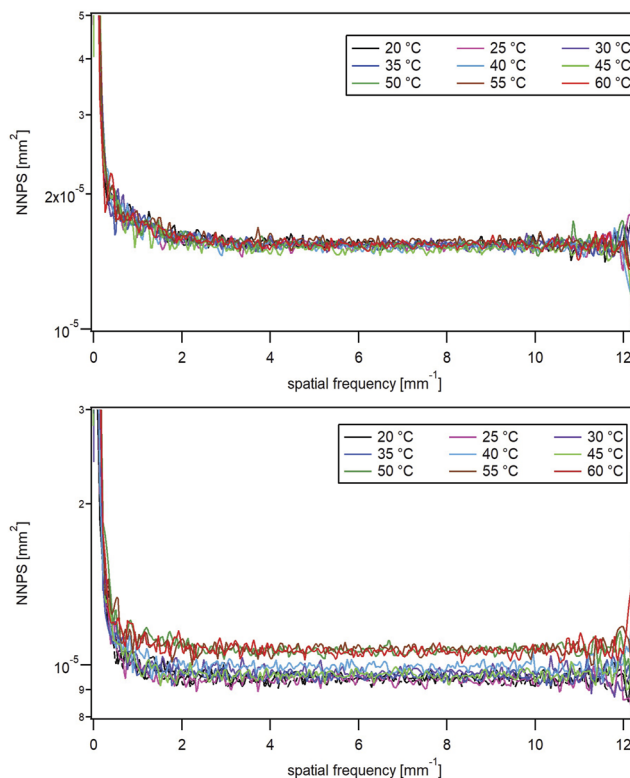

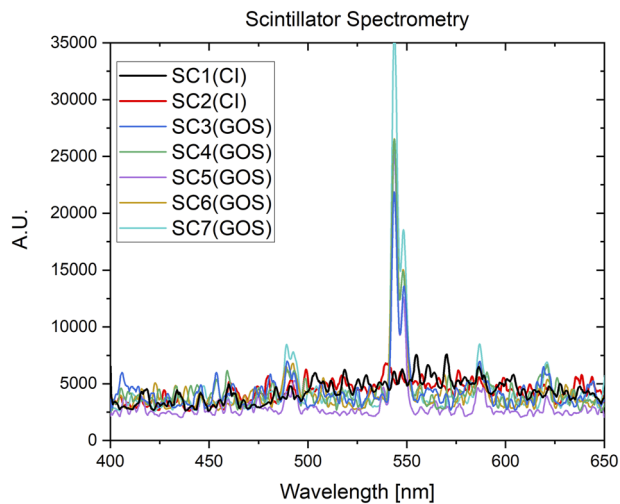**FIG. 7.** NNPS curves for the SC3(GOS) (top) and SC2(CI) (bottom) at different temperatures.

FIG. 6. DQE curve comparison of the tested scintillators @18 μGy.

FIG. 8. Emitted light spectra of the tested scintillators.

FIG. 9. MTF comparison of all lenses, with the SC5(GOS) scintillator and IS1 sensor, RQA5 beam (70 kV and 20 mA s).

5. Performance and cost analysis

The SC1(CI) showed the best image quality among the tested scintillators. However, it has some drawbacks inherent to CsI:Tl scintillators, e.g., higher price, performance decrease at high temperature, and degradation due to humidity[44] (CsI is slightly hygroscopic, i.e., tends to absorb moisture from the air[45]). This can be problematic for their implementation in an x-ray detector intended for low-income tropical countries. The other CsI:Tl scintillator, SC2(CI), exhibited the same drawbacks as the SC1(CI) with a lower image quality.

SC6(GOS) and SC7(GOS) scintillators are cost-effective but showed very poor performances with the exception of a very good DQE(0) for the SC7(GOS). However, this is at the expense of the MTF, which leads to a cutoff frequency below the minimum required for film-screen x-ray detectors intended to medical applications. The SC3(GOS) and SC4(GOS) scintillators (both from the same manufacturer) were the most expensive among the tested Gd_2O_2S:Tb scintillators; however, their performance, both in MTF and DQE, was below average.

The SC5(GOS) outperformed all Gd_2O_2S:Tb scintillators in MTF and DQE {except for the SC7(GOS) at low frequency [DQE(0)]}. In addition, it does not suffer from image quality loss due to high temperature and humidity (Gd_2O_2S:Tb is not hygroscopic[46]). Moreover, it is the most cost efficient of all tested scintillators. This makes it a promising candidate for an x-ray detector intended for low-income tropical countries.

B. Lenses

1. MTF

The measured MTFs for the different lenses are presented in Fig. 9. The MTFs were measured at the center of the image, where the focus of the lens is optimal. Due to Seidel's curvature of field effect, edges of an image tend to be slightly out-of-focus when the center is in focus. This effect depends on the lens characteristics, the size of the object and image, and the focal distance. To determine the effect
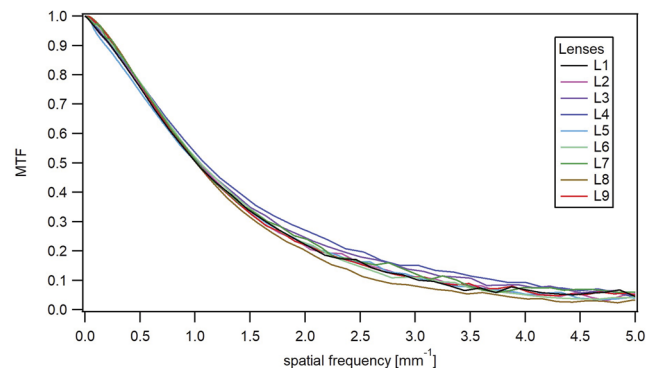
of the out-of-focus aberration, the MTF at the edge of the images was calculated and compared to the center values. As expected, the MTF measured in the edge is lower than the MTF in the center; however, the maximal variations are low (<0.03).

All the characterized lenses show a similar MTF behavior. The 1270XX12MP-M12 lenses slightly outperform the others in terms of spatial resolution, which is surprising given their low price. On the other hand, the German L8 lens has the lowest spatial resolution. Nevertheless, its cutoff frequency (3.75 lp/mm) is still much higher than the minimum required.

2. DQE

The DQE plots of all characterized lenses are shown in Fig. 10.

a. DQE(0) vs focal length. The higher the focal length, the lower the DQE. This is explained by the fact that with a lower focal length, the camera is closer to the scintillator (for imaging the same area); thus, more photons reach the image sensor. Nevertheless, low focal length usually comes with more geometrical aberration for such small size, low cost lenses, i.e., little room for aberration correction.
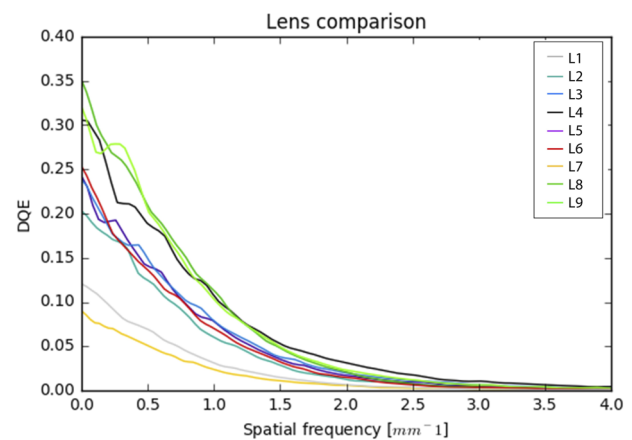

FIG. 10. DQE comparison of all lenses, with the SC5(GOS) scintillator and the IS1 sensor, RQA5 beam (70 kV and 3.10 mA s, 2.5μGy).

Therefore, a trade-off between light collection and image distortion must be carefully defined.

b. DQE(0) vs F-stop. The F-stop is linked to the numerical aperture and the lens entrance pupil. The wider the entrance pupil (or the lower F-stop), the more light can pass through the lens. Therefore, the lower the F-stop, the higher the DQE. However, a higher quality lens with a higher F-stop can have a higher DQE(0) than a lower quality lens with a lower F-stop. Such is the case of the L6 (f 1.6) that has a higher DQE(0) than two of the lenses (L3 and L5) with a lower F-stop (1.2). This shows that, despite the theoretical features described in the data sheet, the lens performances are highly dependent on the quality of manufacturing.

3. Performance and cost analysis

After analyzing the experimental results, lenses with a focal length of 6 mm represent the best trade-off between geometric distortion, field of view, and light throughput. In addition, 6 mm focal length lenses are very common in the market. Therefore, they are easy to obtain, there are many models to choose from, and their prices are low in comparison to more specialized optics.

The L8 lens is the best candidate for the detector system. It gave the best zero-frequency DQE levels from the measured lenses at an acceptable cost. Its main drawback is its low MTF, which, however, remains higher than the minimum required.
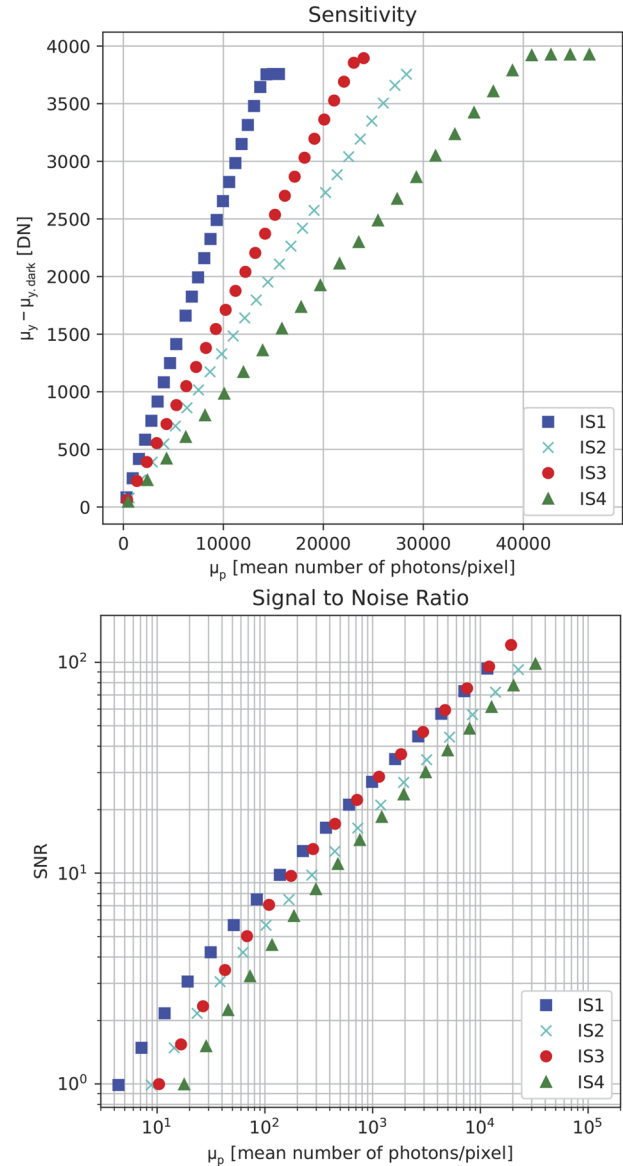
C. Image sensors

The measured sensitivity and SNR plots for all characterized sensors are presented in Fig. 11. For the color sensors, only the green channel was considered (50% of the pixels). Therefore, to account for the loss of sensitivity due to the Bayer filter, the pixel surface was considered to be that of two pixels. Table IV summarizes all the characterized sensors and measured metrics.

1. Sensitivity

The sensor's sensitivity is given by its mean pixel response to light [in digital number (DN)]. The fixed irradiation, wavelength, and exposure time were used to compute the number of photons per pixel for each measured point. All sensors showed linear responses up to saturation. The IS1 [Fig. 11 (top)–dark blue squares] shows the best sensitivity behavior from the measured sensors. This can be explained by the "back-side illuminated" technology used in its design. In "back-side illuminated" sensors, the photodiode is located over the integrated circuit and metal lines (opposite to traditional CMOS sensors); this reduces the light scattering and reflection; thus, more photons reach the photodiode (improving the sensitivity and reducing the noise). The IS2 sensor uses the same technology as the IS1; however, its results are below the monochrome version. This is due to the fact that only 50% of its pixels are able to detect green light (Bayer filter); therefore, half of the photons are lost.

2. SNR

The signal-to-noise ratio (SNR) is computed by dividing the mean value of an image with homogeneous illumination by its standard deviation. The EMVA 1288 standard proposes a camera model with a single internal noise source that is the sum of dark and quantization noise. The number of photons also fluctuates statistically (shot noise); this phenomenon is not negligible for a small number of photons.

FIG. 11. Image sensor characterization results for sensitivity and signal-to-noise ratio (SNR). μ_y is the mean value of light image in the digital value (DN), and $\mu_{y\,dark}$ is the mean value of the dark image in the DN to remove in order to make black equal to 0 (removal of pedestal level).

TABLE IV. Main data results from the sensors' characterization.

Parameter	Unit	IS1	IS2	IS3	IS4
Pixel size	μm	2.90	2 × 2.90	3.75	2 × 3.00
Quantum efficiency	%	75.1	37.8	76.0	29.9
System gain	DN/e$^-$	0.36	0.36	0.22	0.33
Temporal dark noise	e$^-$	2.67	2.71	7.30	4.74
Absolute sensitivity threshold	p	4.38	8.81	10.4	17.8

Results under low light conditions, with a low number of photons, are of most interest for the x-ray detection application. Since it would be difficult to properly measure the SNR with an illumination of only some photons, the EMVA 1288 standard proposes a computation to extrapolate the SNR based on the fitted camera model. The plotted curves correspond to this extrapolation and make the absolute sensitivity threshold visible i.e., absolute sensitivity threshold corresponds to the point where the noise is equal to the signal and, thus, the smallest amount of photons detectable by the camera. Again, the IS1 monochrome [Fig. 11 (bottom)–dark blue squares] shows the best behavior from the characterized sensors, especially under low light condition, thanks to its low-noise technology.

3. Performance analysis

Multiple CMOS sensors were tested according to the EMVA1288 standard. Low light performance is the key factor in selecting the correct sensor for this application. Results showed that the new IS1 outperforms all other tested sensors in that regard. Therefore, it is a good candidate for the multi-camera array x-ray detector.

D. Sensor shielding (lead glass)

In order to reach a good trade-off between x-ray absorbance and light transmittance, different tests were performed, at 20 and 30 mA s, with several Pb equivalent thickness glasses (from 0.5 to 3 mm). Since the lead glass absorption rate depends on the energy of the x-ray photons, three series of tests were performed at 70, 80, and 120 kV. The detection and counting of the direct hits were done with a customized threshold algorithm (Sec. IV C 1).

Placing the lead glass shield in front of the sensor resulted in a dramatic reduction in the number of direct hits: the higher the Pb equivalent thickness, the lower the number of direct hits, i.e., higher x-ray absorption rate, until 1.5 mm where it stabilizes in an average hit reduction of around 93%. The remaining hits can be attributed to the diffusing and back-scattering x-ray photons due to the setup.

The drawback of using a lead glass shield is a reduction in the light transmittance. Transmittance measurements, for a wavelength range from 500 to 600 nm, showed a light absorption of around 7% by the 0.5 mm Pb equivalent thickness, which increases to 14%–16% for the ≥1.5 mm Pb equivalent thicknesses. This absorption will have a direct impact on the DQE, since the cameras will collect less light. However, this loss is considered acceptable in comparison to the benefit of having x-ray shielding to prevent residual x-ray photons to hit the sensor.

These results showed that, with a hit reduction of more than 93% and a reduction in light transmittance of less than 14%, the 1.5 mm Pb equivalent thickness glass is the best option to protect the sensors and other system electronic components from residual x-ray hits.

IV. IMAGE DETECTOR: DESIGN and ARCHITECTURE

The detector architecture consists of multiple multi-camera modules (four cameras per module) that comprise the CMOS image sensors, a computational unit (an FPGA), and memory (SRAM) to buffer the data. A master unit will collect the pre-processed images coming from these multi-camera modules and finalize the
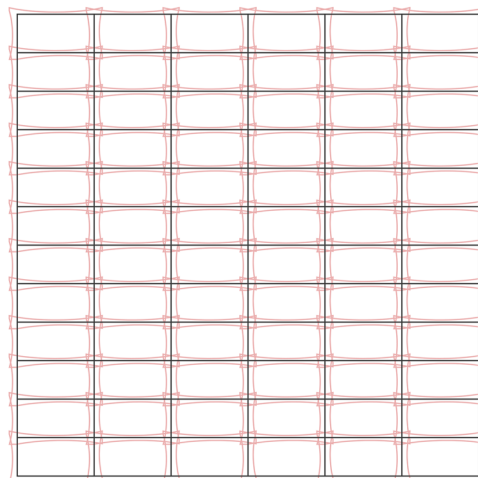

FIG. 12. Sub-image distribution for 6 by 12 cameras.

stitching. Based on the characterization results presented in Secs. I and III, the components showing the best compromise in terms of price, environment resistance, and performances were selected (optimum configuration): the German lens L8, the monochromatic IS1 sensor, and a lead glass of 1.5 mm Pb equivalent thickness. With this configuration, and based on the test results, an optimal scintillator to image a sensor distance of 98.72 mm was determined. Taking into account the geometric distortion correction and the minimum overlap, this results in a matrix of 6 by 12 cameras (72 in total), as depicted in Fig. 12.

A. Image sensors

In an electronic imaging module embedding, the selected image sensor was developed (Figs. 13–15). The 4 × IS1 module embed four IS1 CMOS image sensors and their respective lens holders. Each four-camera module uses the 1 Intel FPGA Cyclone IV EP4CE22F17 chip to buffer the image in a small 32 MB dedicated SRAM memory. Special care was taken to design low noise power supplies and lengths and impedance matched data paths to enhance signal integrity and minimize contribution of the board electronic noise to the sensors. The FPGA includes some pre-processing algorithms to correct the flat image (for structured noise correction) and dark image (for electronic noise correction), by applying the bad
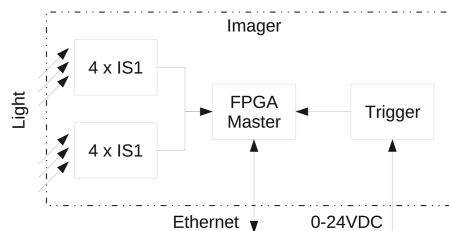

FIG. 13. Block diagram of two imaging modules and the master unit with external connectivity.
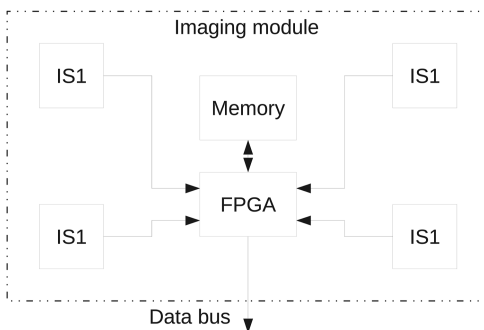
FIG. 14. Block diagram of the architecture of the imaging module with sensors, memory, FPGA, and processor.
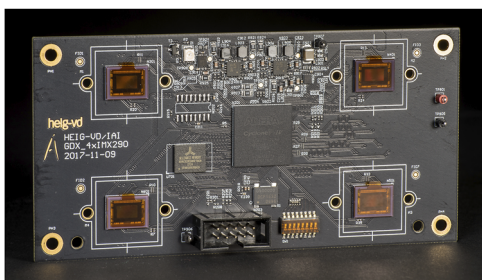

FIG. 15. Module 4 × IS1 (six layers PCB with controlled impedance, BGA components).

pixel correction (Sec. IV C 1) and by averaging series of flat and dark images to reduce the noise impact. The implemented topology enables us to configure gains and exposures of many modules through a single master unit, as well as triggering a simultaneous image capture from all the sensors. The modules are designed to be mounted on a backplane circuit through a high-speed connector system. This structure enables a region of the detector to be easily replaced for maintenance, if need be. Finally, the images are gathered by the FPGA master to be held at disposition of the control computer. Distributing the computing power to multiple modules makes the electronic architecture more complex. However, it also reduces the workload of the master unit and simplifies its interface.

B. Master unit

A demoboard Terasic DE1-SoC was selected as the master unit. The main task of the master unit is to interface all multi-camera modules by configuring the image sensors through the SPI bus. The master unit also triggers all the cameras at the very same time in order to avoid any desynchronization between the sub-images. Once the pre-processed data from the multi-camera unit are retrieved into the master unit, it will finalize the image reconstruction in order to output a reconstructed image to an external PC via Ethernet protocol.

C. Image processing

Each image sensor will produce a *raw image* corresponding to an imaged area of the scintillator, which is affected by a variety of intensity and geometric artifacts. Stitching is the operation that consists in assembling raw images into a final pre-processed image, which should not present any of these artifacts or any observable assembly cues. Strictly speaking, basic (e.g., histogram equalization or edge enhancement) and advanced[47] image post-processing operations are not part of the stitching process, so they are beyond the scope of this paper. The overall stitching process is depicted in Fig. 16.

1. Bad pixel detection and removal

Bad pixels refer to pixels with abnormal intensity, such as dead (always off) or hot (always on) pixels. Such stuck pixels appear progressively over time due to sensor degradation, and their position can be detected and permanently recorded. Hot pixels are also the result of x-ray direct hits not corrected by the sensor shielding solutions. By detecting the bad pixels, we can replace their intensity by a weighted average of their neighboring pixel intensities. Our bad pixel detection is based on the analysis of excessive deviations of pixel intensity in the raw and flat images compared to smoothed versions obtained by median filtering. For instance, the hot pixel detection uses at first a maximum filter that detects in small 3 × 3 image neighborhoods the local maxima. Then, a hot pixel is chosen among these maxima if the difference of its intensity between the original and the smoothed images is larger than a threshold.

2. Dark–flat intensity correction

Based on dark and flat images, raw images are corrected to get rid of the intensity inhomogeneity caused by the vignetting effect—mainly characterized by a light falloff far from the image center. Dark images are acquired in total darkness without x-ray
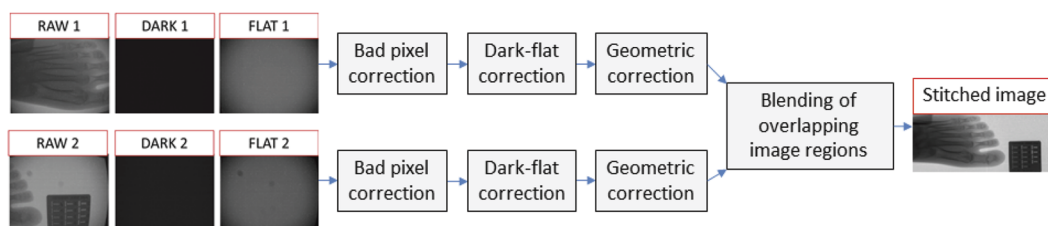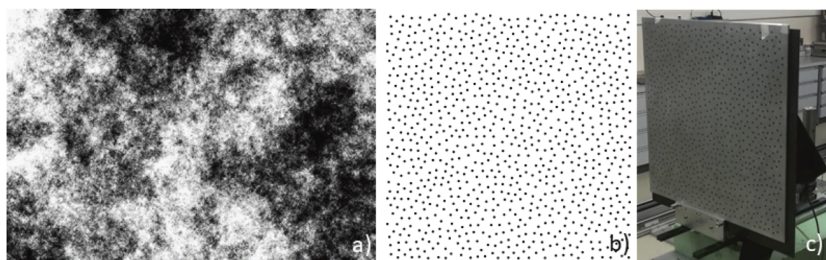

FIG. 16. Overview of the stitching pipeline exemplified with a two camera setup.

FIG. 17. Camera calibration patterns: (a) point cloud pattern used for intrinsic calibration, (b) random dot pattern [50] used to manufacture, and (c) the extrinsic calibration aluminum plate.

emission, while flat images are radiographs acquired without anything in front of the scintillator. The dark–flat correction is simple: $I = k(I_r - I_d)/(I_f - I_d)$, where I_r, I_f, and I_d are the raw, flat, and dark images. Parameter k is a normalizing factor usually computed as the average of all pixel intensities of $(I_f - I_d)$. When correcting images from multiple sensors, the constant k must be identical for all sensors to avoid global intensity inhomogeneity between corrected images I.

3. Geometric correction

Each camera sensor S_i is modeled as a pinhole camera characterized by the estimated intrinsic and extrinsic parameters.[48] Intrinsic parameters include the intrinsic matrix K_i related to the lens characteristics (e.g., focal distance and pixel size) and tangential and radial distortion parameters r_i modeling the non-linear deformation of the lens. Extrinsic parameters express the rigid transform $T_i = (R_i, t_i)$ from a world coordinate system CS_w to a camera coordinate system CS_i, where R_i and t_i are the rotation and translation of the rigid transform.

Intrinsic calibration can be performed for each camera independently and with visible light using a calibration pattern. We selected a point cloud pattern [Fig. 17(a)] from OpenCV library[49] that allows partial visibility of the pattern—a very useful feature given the small field of view and short focal distance of the camera sensors. In the case of extrinsic calibration, we need to ensure that all cameras share the *same* world coordinate system CS_w in order to estimate the spatial positioning and orientation of each camera with respect to each other. This is achieved by using a calibration pattern simultaneously imaged by all cameras and whose parts can be unambiguously detected. The acquisition must be done with *x-ray emission* as the conversion from x rays to visible

light takes place on the plane of the scintillator. Hence, the calibration pattern must not only offer partial detection but should also be x-ray "compatible" and easy to manufacture. In this context, we chose the random dot pattern from Oyamada *et al.*[50] composed of dots [Fig. 17(b)] that can be easily drilled on an aluminum plate [Fig. 17(c)], yielding highly contrasted features in the radiographs.

Based on the estimated calibration parameters, a geometric correction process is applied on each sensor image I_i: (1) image undistortion produces rectified images without lens distortion using intrinsic parameters K_i and r_i; (2) homography transformation converts the rectified image in the common world CS and resamples it to match a desired image resolution. The homography is computed from K_i and extrinsic parameters R_i and t_i. The geometric correction can be seen as an *unwarping* process using deformation maps, which can be pre-processed and applied very efficiently in the hardware (e.g., FPGA).

4. Blending

Unwarped images will present some overlapping regions, as depicted in Fig. 18(a). A successful dark–flat correction coupled with a gain compensation approach[51] will produce consistent image intensities across overlapping regions. This consistency avoids the need to identify frontiers in overlapping regions used to avoid so-called *seam* blending artifacts.[52] Similarly, advanced blending (e.g., multiband blending[53]) is not necessary, and we can apply a simple weighted linear blending (also known as feathering), where weights are computed from distance maps of the unwarped image regions. As a result, the blending is simple, deterministic, and very efficiently executed, yielding excellent stitching results, as depicted in Fig. 18(c). Further examples of x-ray images taken with the
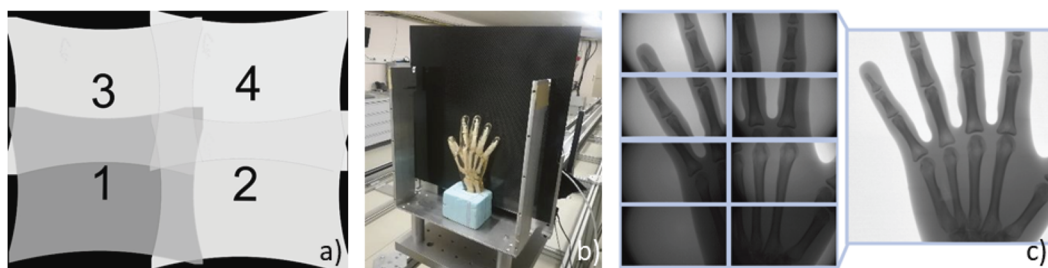
FIG. 18. Blending and stitching: (a) after geometric correction, images will present overlapping areas that will be seamlessly blended into a final stitched image. An example of stitched image of a hand phantom (b) and the produced x-ray image with eight of the detector image sensors is shown in (c).
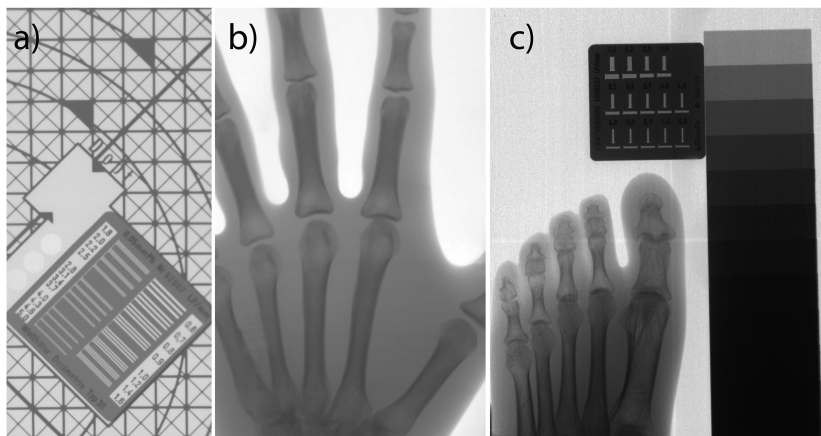
FIG. 19. Examples of x-ray images taken with the developed prototype and processing approach: (a) ETR calibration device (70 kV, 50 mA s), (b) zoomed-in detail of the hand image in Fig. 18 (44 kV, 50 mA s), and (c) foot image with calibration patterns (48 kV, 40 mA s). The central vertical and horizontal bright lines in the right image are not artifacts of the stitching approach, but they represent the projection of metallic wires used to hold together the imaged objects.

developed system and processed with the described approach are presented in Fig. 19.

V. RESULTS

A. Multi-camera module performance

Two types of multi-camera modules were assembled (GDX_IS1_LR and GDX_IS1_SR), implementing linear and switching voltage regulators, respectively. Switching voltage regulators have a higher power efficiency compared to linear regulators, but they can add undesired electronic noise to the system. Both modules were tested with visible light and with x rays.

### B. Visible light characterization

The visible light characterization of the developed multi-camera module was performed with the same method as the image sensor characterization [section characterization (Sec. II E 2) using the setup described in Fig. 4]. The first module to be characterized was the GDX_IS1_SR. In the initial measurements, a line pattern was visible on the image under low light conditions. This pattern was always present but randomly positioned. The pattern is presumably caused by the "line-by-line" method that the integrated analog-to-digital converter uses to read the sensor pixels. Because of the line-wise nature of the process, a small variation of the converter reference voltage could induce a faint line pattern, which is negligible under daylight conditions but can jeopardize the DQE results in x-ray application. A method to quantify this pattern is the Vertical Dark Signal Non-Uniformity (DSNU) as described by the EMVA 1288 3.1 standard.[37] This method can be understood as a vertical Fourier transform that will peak at spatial frequencies corresponding to cyclic line patterns. As expected, the vertical DSNU showed a clear peak corresponding to the pattern spatial frequency in visible light (Fig. 20, red curve).

A second multi-camera module (GDX_IS1_LR) was developed to reduce the high noise levels observed in the first module, maintaining the same architecture but using linear voltage regulators instead of switching voltage regulators. Replacing the voltage regulators highly reduced the observed linear pattern and its frequency peak (Fig. 20, green curve). This improved the resulting

SNR (Fig. 21, green), leading to similar SNR levels to the reference commercial camera (Fig. 21, blue).

C. Temperature and humidity influence

To determine temperature and humidity influence on the developed multi-camera module, the visible light characterization was repeated with the detector inside a climatic chamber under multiple controlled temperature and relative humidity conditions (the whole test setup including light source and integrating sphere was also mounted inside the climatic chamber). The measurements were done at 25 °C (<20% RH), 50 °C (<20% RH), and 50 °C (>90% RH) and compared to the measurement results under room conditions. In order to maintain the exact environmental conditions during all
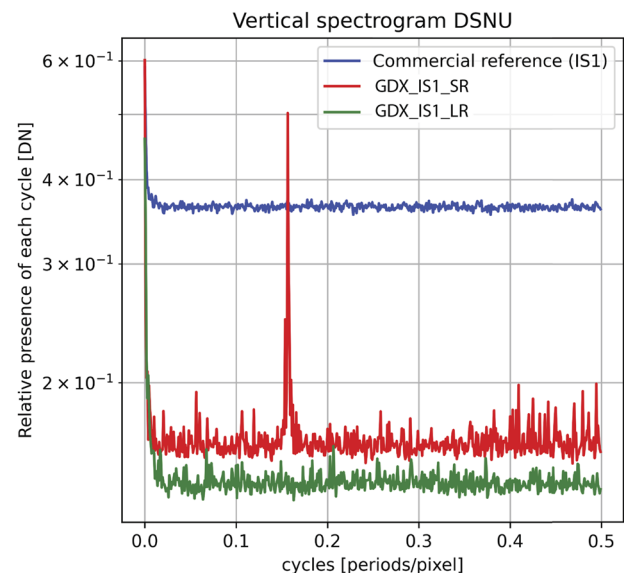
FIG. 20. Dark Signal Non-Uniformity (DSNU) (bottom) plots from the developed GDX_IS1_LR (red) and GDX_IS1_SR (green) multi-camera modules and the reference commercial camera with the IS1 sensor (blue).
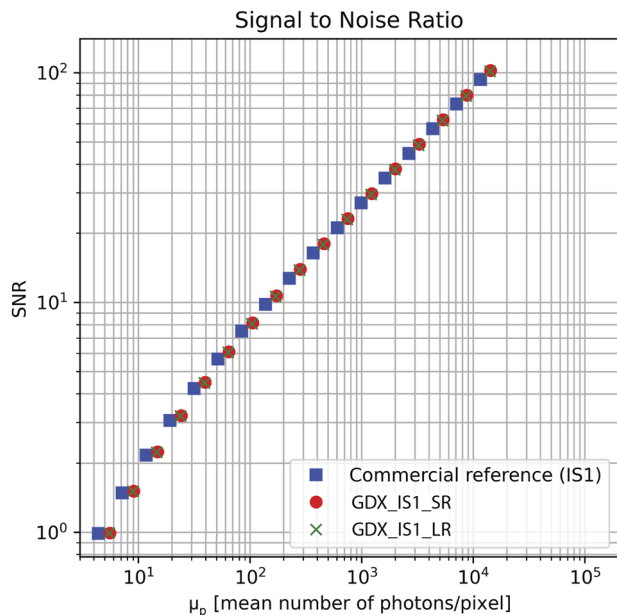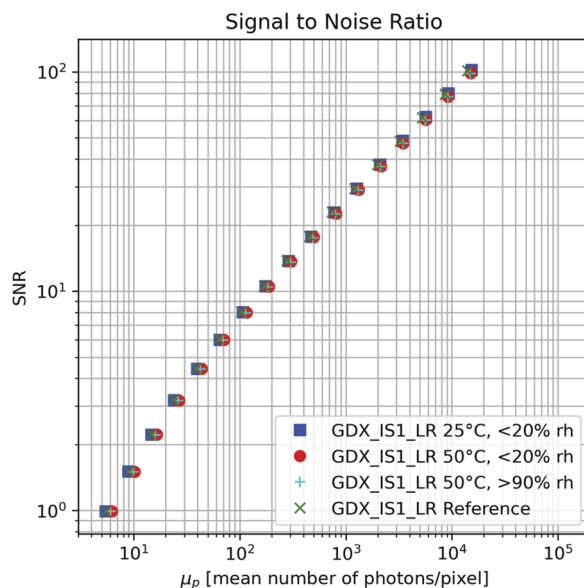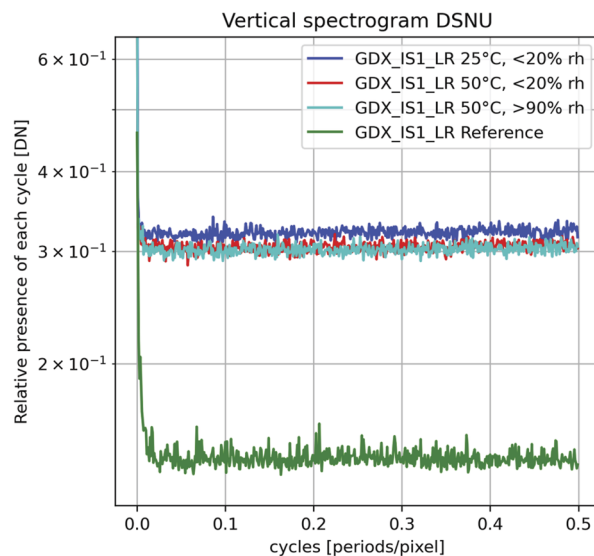
FIG. 21. Signal-to-Noise Ratio (SNR) plots from the developed GDX_IS1_LR (red) and GDX_IS1_SR (green) multi-camera modules and the reference commercial camera with the IS1 sensor (blue).

FIG. 22. Signal-to-Noise Ratio (SNR) (top) and Dark Signal Non-Uniformity (DSNU) (bottom) plots from the developed GDX_IS1 multi-camera modules under room conditions (green), 25 °C and <20% RH (blue), 50 °C and <20% RH (red), and 25 °C and >90% RH (cyan).

the stages of the light characterization measurements, it was decided not to open the chamber to place the sensor cover for the dark image measurement. Thus, the dark image measurements were done under the climatic chamber darkness conditions.

The results show no significant degradation of the signal-to-noise ratio [Fig. 22 (top)]. The vertical spectrogram of dark signal non-uniformity [Fig. 22 (bottom)] exhibits no specific artifacts under the variation of the climatic conditions. Curves corresponding to measurement in the climatic chamber [Fig. 22 (bottom), blue, red, and cyan] have an offset compared to the reference measurement under room conditions [Fig. 22 (bottom), green]. This was caused by the imperfect darkness conditions inside the climatic chamber.

D. X-ray characterization

The developed detector was characterized with the two most promising scintillators identified during the characterization phase, i.e., the SC1(CI) (CsI:Tl) and the SC5(GOS) (Gd_2O_2S:Tb). The DQE was measured for different DAK, between 0.59 and 20 μGy peaks (0.63–20 mA s) at the detector for the RQA5 beam (70 kV), at a frequency of 0.5 mm^{-1} (Fig. 23). The low-frequency fixed pattern noise on the images increased the NPS and decreased the DQE below 0.5 mm^{-1}. The best performance for the developed detector was observed between 0.5 and 5.0 μGy at the detector. The maximal DQE for the SC1(CI) and SC5(GOS) scintillators were around 0.60 and 0.30, respectively, for the reference DAK chosen at 2.34 μGy. The fixed pattern noise increases with the DAK squared and make the low-frequency DQE decreases as a function of the DAK.

The higher DQE obtained with the SC1(CI) scintillator can be explained by its micro-pillar structure and high thickness: CsI:Tl is a crystal that can be grown in vertical micro-pillar structures (2–5 μm diameter, and over 400 μm long) on a plane surface. This helps guiding the light in one direction and avoid lateral scattering; therefore, the MTF is generally better in CsI:Tl scintillators. Gd_2O_2S:Tb is deposited in a powder structure and, therefore, has no light guiding capability, which leads to wide-angle scattering of the visible photons and lower image sharpness.[54]
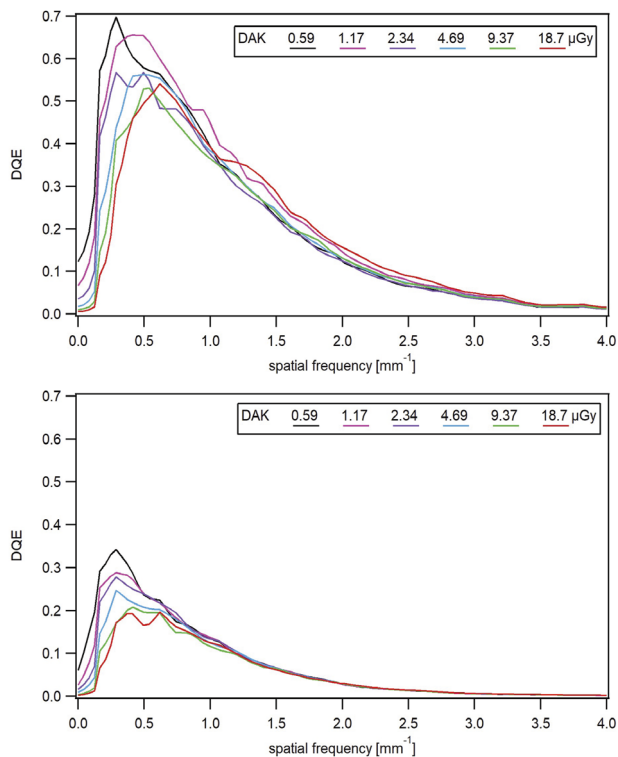
FIG. 23. DQE curves obtained with the developed detector (GDX_IS1_LR) at different DAK. The top plots were obtained with the SC1(CI) scintillator and the ones in the bottom with the SC5(GOS) scintillator.

The light throughput of the scintillator depends on the conversion efficiency for a given x-ray radiation. It is linked to the absorption rate and light yield (also called gain). For a given thickness, CsI:Tl has a higher absorption rate and light yield compared to Gd_2O_2S:Tb. Therefore, the light throughput of CsI:Tl scintillators is higher.[55] Nevertheless, these performances have a cost. Due to its manufacturing complexity (crystal growth) that requires complex and expensive facilities, CsI:Tl scintillators are more expensive than Gd_2O_2S:Tb, especially for a large area (e.g., 430×430 mm^2). Moreover, contrary to CsI:Tl, Gd_2O_2S:Tb has very good chemical durability, mechanical properties, uniformity, and is easier to manufacture.[56]

In sum, compared to the SC1(CI) scintillator, the lower x-ray capture efficiency and x rays to light photon conversion rate of the SC5(GOS) scintillator decrease the low-frequency DQE. The CsI needles of the SC1(CI) scintillator channel the light photons and avoid light spread that occurs in the grain structure of the SC5(GOS). Light spread decreases the spatial resolution and the high-frequency DQE of the SC5(GOS) scintillator.

VI. CONCLUSIONS

A novel, robust, and low cost x-ray imaging system was developed and adapted to the needs and constraints of LMICs. The developed system is based on an indirect conversion chain:

a scintillator plate produces visible light when excited by the x rays, and then, a matrix of the developed multi-camera modules converts the visible light from the scintillator into a set of digital images. The partial images are then unwarped, enhanced, and stitched by specialized software running on a network of FPGAs controlled by a master unit. By implementing a network of FPGA units (instead of a single more powerful processing unit), the partial images can be processed in parallel, reducing the total processing time. Different commercially available components were characterized, and the most suitable were implemented in the fabrication of the detector.

The developed system was characterized at the Institute of Radiation Physics (IRA) from the Lausanne University Hospital [Centre hospitalier universitaire vaudois (CHUV)] using different standard medical radiology measurement setups. The characterization measurements of the developed detector led to high quality x-ray images with DQE levels up to 60% (@2.34 μGy).

The developed detector was designed to overcome common issues of currently available x-ray detectors in LMICs identified during our field (and literature) study. Among the advantages of the developed detector are robustness, low cost, and modularity.

A. Robustness

The detector was designed to withstand the harsh environmental conditions of tropical countries. The characterization results under high temperature (50 °C) and humidity (>90% RH) conditions did not show any significant degradation of the signal-to-noise ratio.

B. Low cost

The use of "off the shelf" components has the advantage of state-of-the-art technologies at a lower cost than customized components. The fabrication costs of the developed detector are between 20% and 50% lower than the flat panel solutions available in the market today; and it is expected that, if mass-produced, the costs will decrease further.

C. Modularity

The implemented modular design allows the system to be easily repaired (by simple replacement of individual modules) without the need of high technical expertise. Additionally, by using "off the shelf" components, the replacement parts can be easily obtained in the market and be replaced at low costs, i.e., in the range of hundreds of USD. Conversely, when the detector from a traditional digital x-ray device breaks, it must be replaced completely by specialized personnel at high costs, i.e., in the range of tens of thousands USD.

However, these advantages come with a cost: due to the lower optical coupling of the implemented architecture, the DQE levels of the developed detector are around 15% lower than the flat panel solutions, i.e., the average DQE levels for commercial flat panels are around 70% (CsI:Tl) and 35% (Gd_2O_2S:Tb), while the DQE levels measured with our detector are 60% (CsI:Tl) and 30% (Gd_2O_2S:Tb). Nevertheless, the measured DQE levels are much higher than other multi-camera systems available in the market (the DQE levels for characterized commercial multi-camera detectors

with CsI:Tl are between 30% and 40%) and the film-based x-ray systems, predominant in low-income countries (the DQE levels of film-based systems are ≤25%[57,58]). Therefore, the developed x-ray detector shows very promising results and potential for being implemented under the context and harsh environmental conditions of LMICs at a lower purchasing and maintenance cost than traditional digital x-ray detectors.

AUTHOR DECLARATIONS

Conflict of Interest

The authors declare that there are no relevant financial or non-financial competing interests to report.

DATA AVAILABILITY

The data that support the findings of this study are available from the corresponding authors upon reasonable request.

REFERENCES

[1]PAHO-WHO, World Radiography Day: Two-Thirds of the World's Population has no Access to Diagnostic Imaging, 2012 (2020 September), available at https://www.paho.org/hq/index.php?option=com_content&view=article&id=7410:2012-dia-radiografia-dos-tercios-poblacion-mundial-no-tiene-acceso-diagnostico-imagen&Itemid=1926&lang=en.

[2]J. Silverstein, Most of the world doesn't have access to X-rays, The Atlantic, 2016.

[3]D. J. Mollura and M. P. Lungren, *Radiology in Global Health: Strategies, Implementation and Applications* (Springer-Verlag, New York, 2014), p. 19, ISBN: 978-1-4614-0603-7.

[4]N. T. Racoveanu, "Medical imaging in the new millennium. How has worldwide health care benefited?," *EMHJ - East. Mediterr. Health J.* **8**(1), 192–204 (2002).

[5]International Atomic Energy Agency, *Worldwide Implementation of Digital Imaging in Radiology: A Resource Guide*, IAEA Human Health Series No. 28 (IAEA Publication, Vienna, 2015).

[6]I. H. Marks *et al.*, "Medical equipment donation in low-resource settings: A review of the literature and guidelines for surgery and anaesthesia in low-income and middle-income countries," *BMJ Global Health* **4**, e001785 (2019).

[7]S. Inglin, (Producer & Director), EssentialMed Foundation (Co-producer), X-Ray Machines: Africa's Broken System (2019). (Video file), available at https://essentialtech.center/x-ray-machines-africas-broken-system/; accessed August 5, 2021.

[8]S. Makohliso, B. Klaiber, R. Sahli, J. R. M. Tapouh, S. N. Amvene, B. Stoll, and K. Schönenberger, "Medical technology innovation for a sustainable impact in low- and middle-income countries: A holistic approach," (published online, 2020).

[9]D. Norman and E. Spencer, Community-based, human-centered design, jnd.org (1 January 2019), available at https://jnd.org/community-based-human-centered-design/; accessed August 6, 2021.

[10]M. A. Chavarria, A. Mugeere, K. Schönenberger, S. Hurst, and M. Rivas Velarde, "Design approaches for creating person-centered, context-sensitive, and sustainable assistive technology for personal mobility in the global south," in *Accessible Technology and the Developing World*, edited by J. Lazar and M. Stein (Oxford University Press, 2021).

[11]K. Shonengerger and S. Makohliso, Technology innovation for sustainable development. edX, available at https://learning.edx.org/course-v1:EPFLx+Innov4DevX+1T2017/home; accessed August 6, 2021.

[12]E. L. Nickoloff, "AAPM/RSNA physics tutorial for residents: Physics of flat-panel fluoroscopy systems," RadioGraphics **31**(2), 591–602 (2011).

[13]A. C. Konstantinidis *et al.*, "The Dexela 2923 CMOS X-ray detector: A flat panel detector based on CMOS active pixel sensors for medical imaging applications," Nucl. Instrum. Methods Phys. Res., Sect. A **689**, 12–21 (2012).

[14]*Digital Mammography*, edited by U. Bick and F. Diekmann (Springer, Berlin, 2010).

[15]Varex Imaging, Medical flat panel detectors, available at https://www.varex imaging.com/products/medical/medical-flat-panel-detectors; accessed August 5, 2021.

[16]Hamamatsu, X-ray flat panel sensors for radiology, available at https://www.hamamatsu.com/eu/en/product/optical-sensors/image-sensor/x-ray-flat-panel-sensor/x-ray-flat-panel-sensors-for-radiology/index.html; accessed August 5, 2021.

[17]C. R. Smith and J. W. Erker, "Low-cost, high-resolution x-ray detector system for digital radiography and computed tomography," Proc. SPIE **2009**, 31 (1993).

[18]B. K. Cha *et al.*, "Performance studies of a monolithic scintillator-CMOS image sensor for X-ray application," Nucl. Instrum. Methods Phys. Res., Sect. A **591**, 113 (2008).

[19]G. H. Gelinck *et al.*, "X-ray detector-on-plastic with high sensitivity using low cost, solution-processed organic photodiodes," IEEE Trans. Electron Devices **63**(1), 197–204 (2016).

[20]H. K. Kim *et al.*, "Development and evaluation of a digital radiographic system based on CMOS image sensor," IEEE Trans. Nucl. Sci. **48**(3), 662–666 (2001).

[21]H. K. Kim *et al.*, "Development of a lens-coupled CMOS detector for an X-ray inspection system," Nucl. Instrum. Methods Phys. Res., Sect. A **545**, 210–216 (2005).

[22]JPI Healthcare Solutions, IONA Digital X-Ray PSA Detector Datasheet, available at https://www.jpihealthcare.com/wp-content/uploads/2017/05/IONA_A4_EN_v4_JPI-Healthcare_Website.pdf; accessed August 5, 2021.

[23]JPI Healthcare Solutions, IONA2 Digital X-Ray PSA Detector Datasheet, available at http://www.jpihealthcare.com/wp-content/uploads/2017/05/IONA2_website.pdf; accessed August 5, 2021.

[24]A. D. A. Maidment and M. J. Yaffe, "Analysis of the spatial-frequency-dependent DQE of optically coupled digital mammography detectors," Med. Phys. **21**, 721 (1994).

[25]M. J. Flynn *et al.*, "Quantum noise in digital X-ray image detectors with optically coupled scintillators," IEEE Trans. Nucl. Sci. **43**(4), 2320–2325 (1996).

[26]Z. Jing *et al.*, "Detective quantum efficiency of a CsI:T1 scintillator based scanning slot x-ray detector for digital mammography," Proc. SPIE **3336**, 583 (1998).

[27]RF System Lab, NAOMI X-ray Sensor Specifications, available at http://rfsystem lab.com/en/product/medical/naomi/index.html; accessed August 5, 2021.

[28]Weather Atlas, Monthly weather forecast and climate, available at https://www.weather-atlas.com/en/climate; accessed August 5, 2021.

[29]Arizona State University, WMO region I (Africa): Highest temperature, World meteorological organization's world weather & climate extremes archive, available at https://wmo.asu.edu/content/africa-highest-temperature; accessed August 5, 2021.

[30]World Bank Group, Climate change knowledge portal, available at https://climateknowledgeportal.worldbank.org/country/burkina-faso/climate-data-historical; accessed August 5, 2021.

[31]M. Haddad, Mapping the hottest temperatures around the world, Al Jazeera. 1 July 2021, available at https://www.aljazeera.com/news/2021/7/1/interactive-mapping-hottest-temperatures-around-world; accessed August 5, 2021.

[32]World Meteorological Organization, World Weather Information Service, available at https://worldweather.wmo.int/en/city.html?cityId=1514; accessed August 5, 2021.

[33]BBC, BBC weather, available at https://www.bbc.com/weather/2224827; accessed August 5, 2021.

[34]W. R. Leo, *Techniques for Nuclear and Particle Physics Experiments*, 2nd ed. (Springer, 1994), ISBN: 978-3540572800.

[35]V. B. Mikhailik and H. Kraus, "Scintillators for cryogenic applications: State-of-art," J. Phys. Stud. **14**(4), 4201–4206 (2010).

[36]Laird Thermal Systems, Thermoelectric Cooling for CMOS Sensors, Laird Thermal Systems Application Note, April, 2019

[37]European Machine Vision Association, EMVA Standard 1288: Standard for Characterization of Image Sensors and Cameras, Release 3.1 December 30 (2016).

[38]ICRU Report 54 1996 Medical imaging—The assessment of image quality. J ICRU os 28, https://doi.org/10.1093/jicru/os28.1.Report54.

[39]IEC, Medical electrical equipment–characteristics of digital X-ray imaging devices–Part 1-1: Determination of the detective quantum efficiency–detectors used in radiographic imaging, IEC 62220-1-1:2015.

[40]R. M. Nishikawa, The Fundamentals of MTF, Wiener Spectra, and DQE (2020 September), available at https://www.aapm.org/meetings/99am/pdf/2798-87374.pdf.

[41]I. A. Cunningham and A. Fenster, "A method for modulation transfer function determination from edge profiles with correction for finite-element differentiation," Med. Phys. **14**, 533 (1987).

[42]J. M. Sandrik and R. F. Wagner, "Absolute measures of physical image quality: Measurement and application to radiographic magnification," Med. Phys. **9**, 540 (1982).

[43]P. Yang et al., "Effect of humidity on scintillation performance in Na and Tl activated CsI crystals," IEEE Trans. Nucl. Sci. **61**(2), 1024–1031 (2014).

[44]Saint-Gobain Crystals and Detectors, Handling and Care of Crystal Scintillation Detectors, The Netherlands (2020 September), available at https://www.crystals.saint-gobain.com/sites/imdf.crystals.com/files/documents/handling-and-care-of-crystal-scintillation-detectors_70413.pdf.

[45]Saint-Gobain Crystals and Detectors, CsI(Tl), CsI(Na) Cesium Iodide Scintillation Material, The Netherlands (2020 September), available at https://www.crystals.saint-gobain.com/sites/imdf.crystals.com/files/documents/csitl-and-na-material-data-sheet.pdf.

[46]C. W. E. van Eijk, "Inorganic scintillators in medical imaging," Phys. Med. Biol. **47**, R89 (2002).

[47]S. Dippel, M. Stahl, R. Wiemker, and T. Blaffert, "Multiscale contrast enhancement for radiographies: Laplacian pyramid versus fast wavelet transform," IEEE Trans. Med. Imaging **21**(4), 343–353 (2002).

[48]Z. Zhang, "A flexible new technique for camera calibration," IEEE Trans. Pattern Anal. Mach. Intell. **22**(11), 1330–1334 (2000).

[49]G. G. Bradski and A. Kaehler, OpenCV. Dr. Dobb's journal of software tools, 3, 2000.

[50]Y. Oyamada, P. Fallavollita, and N. Navab, "Single camera calibration using partially visible calibration objects based on random dots marker tracking algorithm," in The IEEE and ACM International Symposium on Mixed and Augmented Reality, Workshop on Tracking Methods and Applications (TMA), Atlanta, 2012.

[51]M. Brown and D. G. Lowe, "Automatic panoramic image stitching using invariant features," Int. J. Comput. Vision **74**(1), 59–73 (2007).

[52]V. Kwatra, A. Schödl, I. Essa, G. Turk, and A. Bobick, "Graphcut textures: Image and video synthesis using graph cuts," ACM Trans. Graphics **22**(3), 277–286 (2003).

[53]P. J. Burt and E. H. Adelson, "A multiresolution spline with application to image mosaics," ACM Trans. Graphics **2**(4), 217–236 (1983).

[54]K. C. Bo et al., "Fabrication and comparison $Gd_2O_2S(Tb)$ and $CsI(TI)$ films for X-ray imaging detector application," in 2008 IEEE Nuclear Science Symposium Conference Record, NSS/MIC (IEEE, 2008), pp. 1232–1235.

[55]T. T. Farman et al., "Effects of scintillator on the detective quantum efficiency (DQE) of a digital imaging system," Oral Surg., Oral Med., Oral Pathol.Oral Radiol. Endod. **101**(2), 219–223 (2006).

[56]I. D. Jung et al., "Flexible Gd_2O_2S:Tb scintillators pixelated with polyethylene microstructures for digital x-ray image sensors," J. Micromech. Microeng. **19**(1), 015014 (2009).

[57]P. Willems, P. Soltani, and B. Vaessen, "Image quality comparison of digital radiographic systems for NDT," in Proceedings of the 15th World Conference on Non-Destructive Testing, Rome, 15–21 October 2000, available at https://www.ndt.net/article/wcndt00/papers/idn421/idn421.htm.

[58]M. Spahn, "Flat detectors and their clinical applications," Eur. Radiol. **15**(9), 1934–1947 (2005).